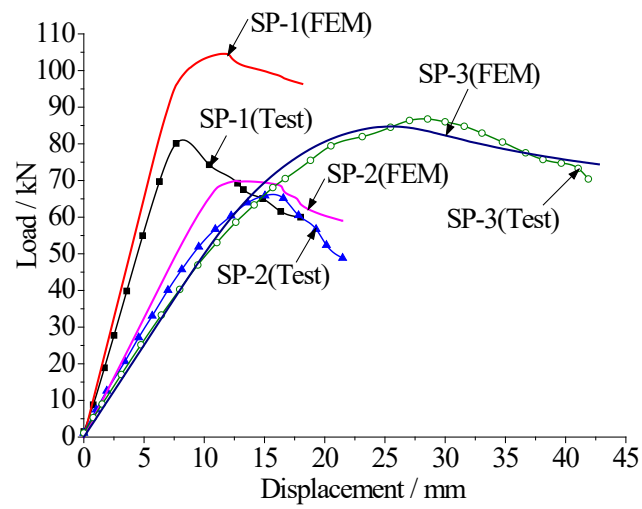


Journal of Constructional Steel Research

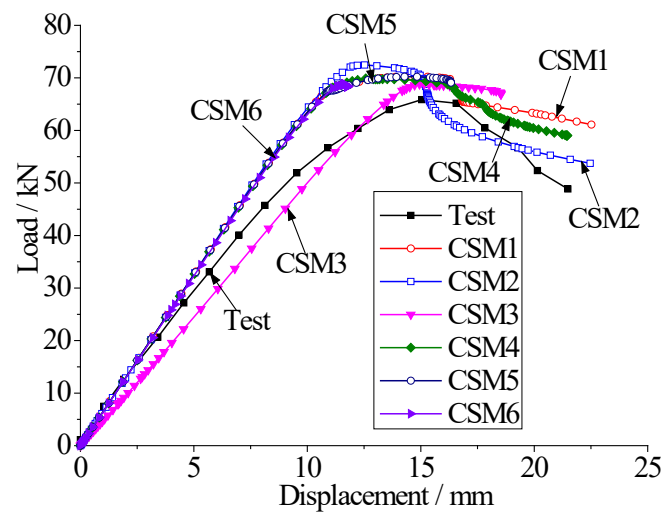
Research on Local Buckling of Stainless Steel Lipped C-Section Beam around Strong-axis --Manuscript Draft--

Manuscript Number:	JCSRES-D-20-00808
Article Type:	Research Paper
Keywords:	Stainless steel beam, Lipped C-section, Local buckling, Strong axis bending, Simplified model
Manuscript Region of Origin:	Asia Pacific
Abstract:	<p>To study the local buckling capacity of stainless steel beams with lipped C-sections under strong axial bending, tensile tests were performed on 12 stainless steel coupons based on S30408 austenitic stainless steel (AISI304) in flat and corner areas, and mechanical properties and stress-strain curves were obtained. Then, local buckling bearing capacity tests were performed on 6 specimens of stainless steel beams under strong axial bending to determine their mechanical properties and failure mechanism. The failure phenomenon, load-displacement curve, load-strain curve and local buckling bearing capacity were determined. Results show that the failure modes of the specimens are local buckling failure of the flange and web at mid-span. Additionally, a refined finite element analysis model was developed using Python and ABAQUS to simulate and analyse the mechanical performance and local buckling bearing capacity. Then, the analytical results were compared to the test results, and the accuracy of the refined model was verified. Then, the refined model of the stainless steel C-section beam was simplified including the constraint simplification model, which considered different flange constraints and initial imperfections, and the length simplification model, which was based on different length and support constraints. The comparative analysis results showed that the constraint simplification model can simulate the local buckling failure mode more accurately than other models. Additionally, initial imperfections were shown to have little effect on the local buckling bearing capacity; however, specimen length and the bearing constraint condition did affect the local buckling capacity.</p>





Comparison of load-displacement curve between test and finite element results



Comparison of load-displacement curve between CSM and test results of SP-2

Research on Local Buckling of Stainless Steel Lipped C-Section Beam around Strong-axis

Shenggang Fan¹, Hang Zhou¹, Zhixia Ding², Chenxu Li¹, Qinglin Jiang³

¹*School of Civil Engineering, Southeast University, Nanjing 210096, PR China*

²*Dept. of Civil and Environmental Engineering, University of Connecticut, Storrs, Connecticut 06269.*

³*Jiangsu Dongge Stainless Steel Ware Co., Ltd*

ABSTRACT

To study the local buckling capacity of stainless steel beams with lipped C-sections under strong axial bending, tensile tests were performed on 12 stainless steel coupons based on S30408 austenitic stainless steel (AISI304) in flat and corner areas, and mechanical properties and stress-strain curves were obtained. Then, local buckling bearing capacity tests were performed on 6 specimens of stainless steel beams under strong axial bending to determine their mechanical properties and failure mechanism. The failure phenomenon, load-displacement curve, load-strain curve and local buckling bearing capacity were determined. Results show that the failure modes of the specimens are local buckling failure of the flange and web at mid-span. Additionally, a refined finite element analysis model was developed using Python and ABAQUS to simulate and analyse the mechanical performance and local buckling bearing capacity. Then, the analytical results were compared to the test results, and the accuracy of the refined model was verified. Then, the refined model of the stainless steel C-section beam was simplified including the constraint simplification model, which considered different flange constraints and initial imperfections, and the length simplification model, which was based on different length and support constraints. The comparative analysis results showed that the constraint simplification model can simulate the local buckling failure mode more accurately than other models. Additionally, initial imperfections were shown to have little effect on the local buckling bearing capacity; however, specimen length and the bearing constraint condition did affect the local buckling capacity.

Keywords

Stainless steel beam, Lipped C-section, Local buckling, Strong axis bending, Simplified model

1. Introduction

Stainless steel lipped C-section beams are a type of cold-formed thin-walled open section member that typically exhibit three basic buckling modes: local buckling, distortional buckling and global buckling. Under certain conditions, several buckling modes may be coupled. Local buckling is a common problem in cold-formed thin-walled stainless steel members. For stainless steel C-section beams under strong axial bending, local buckling may first appear in the compressed flange or in the compressed area of the web with a large height thickness ratio due to the gradient distribution of stress on the web.

There have been many studies of local, distortional, global and interactive buckling of cold-formed thin-walled open section members; however, related research results primarily focus on ordinary carbon steel members [1-10]. Currently, research on stainless steel members primarily focuses on the mechanical properties and stability performance of closed section members. Results describing the local, distortional, global and interactive buckling of open section members are generally lacking, particularly the basic buckling of stainless steel C-section beams, which are scarce. Gardner and Nethercot [11] experimentally studied the bearing capacity of 37 short columns and 22 pin-ended long columns, and proposed a new method for calculating the bearing capacity of axial compression columns. Lecce and Rasmussen [12, 13] conducted distortional buckling tests and finite element analysis on austenitic and ferritic stainless steel columns with lipped channel sections, and proposed direct strength equations. Feng and Young [14, 15] conducted an experimental study of the web buckling of stainless steel members with lipped channel sections and cold-formed box sections. Results were compared to the stainless steel codes of various countries, and a formula for calculating the buckling strength of the web was proposed. Becque and Rasmussen [16, 17] studied the local and

1 global buckling of austenitic and ferritic stainless steel columns with lipped channel sections. Rossi et
2 al. [18, 19] performed experimental and numerical investigations of the interactive distortional and
3 global flexural-torsional buckling of cold-formed stainless steel columns with lipped channel sections,
4 and a new direct strength method was proposed. Yuan [20] conducted an experimental study and finite
5 element analysis of the local buckling and local-global interactive buckling performance of stainless
6 steel welded I-section and box-section columns and proposed a direct strength method formula for the
7 buckling bearing capacity. Niu et al. [21, 22] performed experimental research and finite element
8 parametric analysis of 6 I-beams with lateral restraints and 24 I-beams without lateral restraints under
9 pure bending conditions. Results indicated that the slenderness ratio and length are the primary factors
10 that affect the bearing capacity of the member. Fan et al. [23, 24] conducted an experimental study of
11 the bearing capacity of S30408 austenitic stainless steel short columns with lipped C-sections and
12 proposed a formula for the direct strength method to describe the bearing capacity of stainless steel
13 short columns.

14 Based on these studies, the local buckling failure mode and ultimate bearing capacity of stainless
15 steel lipped C-section beams under strong axial bending are investigated, using experimental research
16 and finite element numerical simulation analysis of 6 beam specimens of S30408 austenitic stainless
17 steel (AISI304). The failure process and mechanism of the local buckling process were described with
18 a local buckling test, and the test phenomenon, load-displacement curve, load-strain curve and local
19 buckling bearing capacity of each specimen were determined. Additionally, a refined finite element
20 analysis model was developed. Concurrently, to simplify the calculation, a constraint simplification
21 model and a length simplification model were developed to combine different constraints and initial
22 imperfections. The results from the simplified model, refined model and experiments were compared

to verify the accuracy of the simplified model. Finally, a simplification model was proposed to describe the local buckling of lipped C-section stainless steel beams under strong-axis bending.

2. Mechanical properties test

The material used in this test was S30408 austenite stainless steel (AISI304). The cross-section was cold-formed lipped C-section and the section sizes of the specimens were C250×75×20×2.0 and C250×75×20×2.5. In order to obtain the mechanical properties and stress-strain curves of stainless steel, and examine the effect of material hardening in the corner area on the mechanical properties of stainless steel, standard tensile tests in the flat and corner area were conducted respectively.

The test results of the mechanical properties of all coupons are shown in Table 1. The following conclusions can be drawn from Table 1: (1) The elastic modulus of stainless steel is about 1.9×10^5 N/mm², and the test results of the coupons in the flat and corner area are similar. (2) The thickness of the coupon has little effect on the nominal yield strength of stainless steel in the flat area, but has a certain effect in the corner area. The thickness of the coupon affects the ultimate strength of stainless steel both in the flat and corner area. (3) After cold working, the nominal yield strength and ultimate strength of stainless steel in the corner area are significantly improved relative to stainless steel in the flat area, and the post-break elongation is reduced.

Table 1. Test results of mechanical properties of all coupons

Location	Specimen number	t/mm	E_0 / N/mm ²	$\sigma_{0.2}$ / N/mm ²	$\sigma_{1.0}$ / N/mm ²	σ_u / N/mm ²	$\varepsilon_{t0.2}$	$\varepsilon_{t1.0}$	n	δ
Flat area	F-2.0-1	t=2.0	188084	267.04	300.40	732.98	0.00342	0.01160	8.43	58.13%
	F-2.0-2		205195	265.09	302.47	713.46	0.00329	0.01147	4.74	53.75%
	F-2.0-3		195327	268.18	302.35	713.76	0.00337	0.01155	6.43	53.75%
	F-2.5-1	t=2.5	157915	268.81	305.91	751.09	0.00370	0.01194	7.78	51.25%
	F-2.5-2		184731	269.09	304.15	743.03	0.00346	0.01165	7.31	51.88%
	F-2.5-3		191021	263.19	301.64	744.87	0.00338	0.01158	5.55	52.50%
Corner area	C-2.0-1	t=2.0	181727	395.71	475.04	800.11	0.00418	0.01261	4.43	45.00%

	C-2.0-2		196749	389.52	475.95	801.81	0.00398	0.01242	3.88	45.00%
	C-2.0-3		197309	397.71	476.27	799.99	0.00402	0.01241	5.47	44.25%
	C-2.5-1		169366	426.23	515.02	847.92	0.00452	0.01304	5.13	43.00%
	C-2.5-2	t=2.5	172982	419.98	507.43	842.25	0.00443	0.01293	4.91	43.00%
	C-2.5-3		187121	430.20	517.21	841.91	0.00430	0.01276	5.98	44.00%

Notes: (1) The specimen numbers are F-X-Y and C-X-Y; where F is the flat area specimen, C is the corner area specimen, X is the specimen thickness, and Y is the specimen number. (2) t is the specimen thickness; E_0 is the initial elastic modulus of stainless steel; $\sigma_{0.2}$ is the nominal yield stress; $\sigma_{1.0}$ is the stress value corresponding to the residual deformation value of 1.0%; σ_u is the ultimate stress value; $\varepsilon_{0.2}$ is the strain value corresponding to the stress value $\sigma_{0.2}$; $\varepsilon_{1.0}$ is the strain value corresponding to the stress value $\sigma_{1.0}$; $n = \ln(20)/\ln(\sigma_{0.2}/\sigma_{0.01})$ is the hardening index; δ is the post-break elongation. (3) For the specimens F-2.5-1, C-2.0-1 and C-2.5-3, the slip phenomenon occurs during the tensile process, leading to some errors in the test results, so the test results of these three specimens are discarded in the subsequent analysis.

3. Local buckling test under strong axis bending

3.1 Design of Specimen

3.1.1 Local buckling failure conditions

To ensure that local buckling occurs before distortional buckling, additional constraints are set on the compressed flange of the specimen to increase the distortional buckling bearing capacity without changing the local buckling bearing capacity.

Haidarali and Nethercot [25] analysed and calculated the buckling modes of bending members with compressed flanges constrained by different spring stiffnesses. Results showed that an increase in spring stiffness transforms the minimum buckling mode from distortional to local buckling under elastic conditions. Cheng [26] proposed that an appropriate number of profiled steel sheets can be firmly connected with the compressed flange of a C-section beam via self-tapping screws to increase the constraint stiffness of the compressed flange, which in turn restricts the occurrence of distortional buckling.

Based on these results, a profiled steel sheet was used as the elastic constraint and was firmly connected with the compressed flange using a self-tapping screw to ensure local buckling failure. After

1 calculation, the distance l_{scr} of the self-tapping screw along the length of the specimen was set to 225
2 mm to limit the early occurrence of distortional buckling. To determine the local buckling failure mode
3 and bearing capacity of the specimen in the free state, a length of twice the local buckling and half the
4 wavelength was reserved in the middle section along the length direction, where no profiled steel sheet
5 was set up.

6 3.1.2 Section size of specimen

7 The buckling failure mode is determined by its elastic buckling load, which is related to factors
8 such as its section size, length, and restraints at both ends.

9 After analysis and comparison, to facilitate the actual processing of the specimen, six cross-
10 sections were finally selected, and each specimen is composed of two identical C-section members.
11 The section form and number of the components are shown in Fig.1 (a), the cross-sectional dimensions
12 and lengths of the two components were exactly the same. In the Fig.1 (a), MB denotes the component
13 that constitutes the strong axis bending specimen, n is the component number, and A and B are used
14 to distinguish the two components of the strong axis bending specimen. Refer to Table 2 for the
15 grouping number, component number and detailed dimensions of the specimen. The meaning of each
16 parameter in the table is shown in Fig.4 (b).

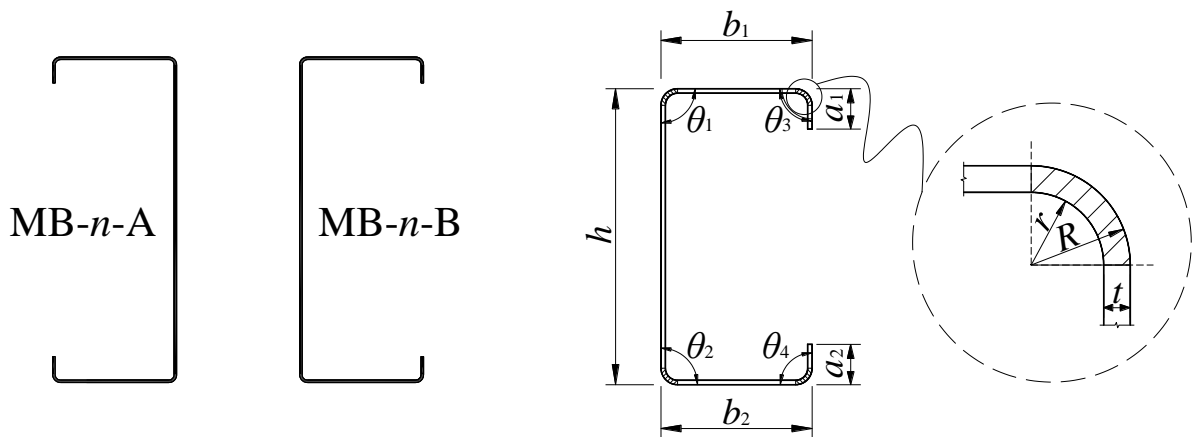


Fig.1 Section shape and parameter of specimen

Table 2. Number, components and geometric parameters of specimens

Specimen number	Component	Section size	h/mm	b_1/mm	b_2/mm	a_1/mm	a_2/mm	t/mm	$\theta_1/^\circ$	$\theta_2/^\circ$	$\theta_3/^\circ$	$\theta_4/^\circ$
SP-1	MB-1-A	C400×90×20×2.0	400	90.46	90.25	19.88	19.54	1.78	90.3	90.2	89.2	92.3
	MB-1-B	C400×90×20×2.0	401	90.06	90.26	20.25	19.82	1.79	90.3	90.2	89.4	89.7
SP-2	MB-2-A	C300×80×20×2.0	302	79.83	80.01	19.74	19.53	1.79	89.5	91.0	89.0	92.1
	MB-2-B	C300×80×20×2.0	300	80.37	80.64	19.81	20.03	1.81	90.5	90.3	89.5	89.5
SP-3	MB-3-A	C250×75×20×2.5	252	75.75	74.83	20.03	19.73	2.29	90.6	88.5	88.3	87.8
	MB-3-B	C250×75×20×2.5	252	75.54	75.53	19.57	19.59	2.30	91.9	91.4	86.7	86.7
SP-4	MB-4-A	C250×75×20×2.0	251	75.36	74.99	20.11	19.84	1.83	90.7	90.7	89.4	89.2
	MB-4-B	C250×75×20×2.0	250	75.55	75.32	20.14	20.11	1.81	91.0	90.1	88.9	89.6
SP-5	MB-5-A	C250×50×20×2.0	250	50.07	50.09	20.39	19.51	1.80	89.3	90.8	88.9	89.3
	MB-5-B	C250×50×20×2.0	250	50.86	50.62	20.15	19.81	1.79	90.2	90.4	89.2	89.0
SP-6	MB-6-A	C150×60×20×2.0	150.5	60.13	60.31	20.09	20.3	1.79	90.5	90.2	89.2	89.6
	MB-6-B	C150×60×20×2.0	151	60.06	59.85	20.41	20.08	1.76	90.1	90.4	89.6	89.3

Note: (1) The length of the specimen $L = 3980\text{mm}$, the inner radius of the corner $r = 2\text{mm}$; (2) The cross-sectional dimension adopts C-section height (h) × flange width (b) × seam width (a) × thickness (t).

3.1.3 Setting of double C-section of specimen

The length of the specimen was selected to be 3600 mm. Considering the connection between the specimen and the support, the length was extended 200 mm towards both sides of the support; thus, the length of the entire specimen was 4000 mm, as shown in Fig. 2

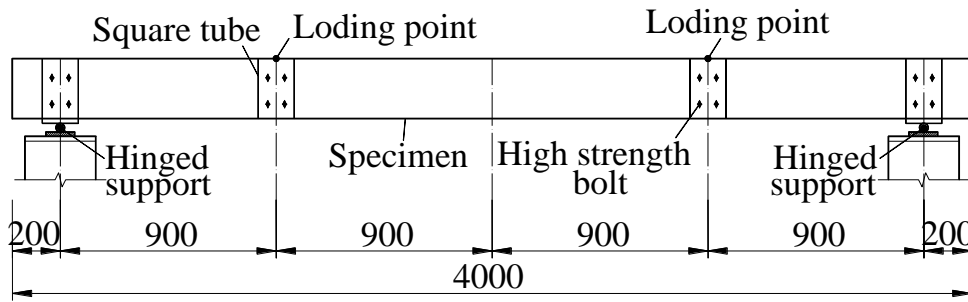


Fig.2 Length of specimen

For the lipped C-section beam, the cross-sectional form is uniaxially symmetric, and the section shear centre is located outside the web plane. To facilitate loading and prevent torsion of the specimen section, two C-section members are assembled back-to-back into double C-section specimens for the

strong axial bending test. Concurrently, square tubes are set at both ends and loading points, and the two C-section members are connected with the square tube through high-strength bolts to ensure that the two C-section members work together, as shown in Fig. 3. The section size of the square tube is chosen to be a box of 150×150×10. At the loading point, the vertical length of the square tube is equal to the height of the cross-section of the specimen to ensure uniform loading, as shown in Fig.3 (a). At the ends, the vertical length of the square tube is 20 mm higher than that of the specimen to prevent local bearing damage, as shown in Fig.3 (b).

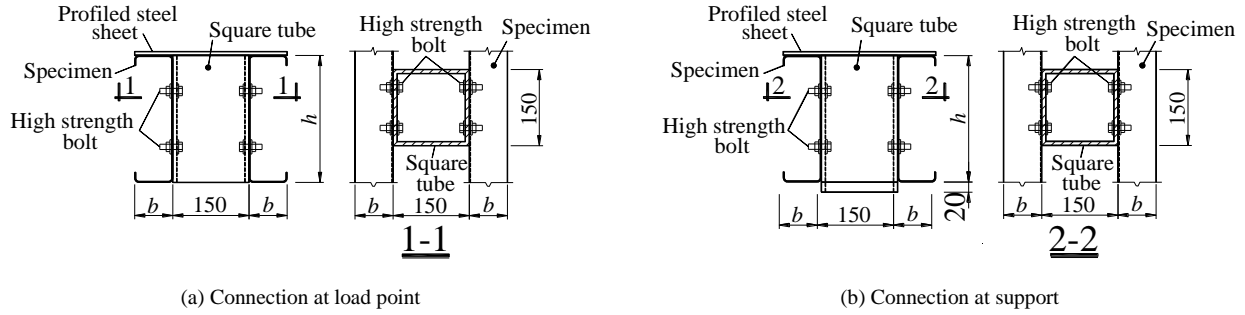


Fig.3 Double C-section specimens

3.2 Initial geometric imperfections

The initial geometric imperfections have an important influence on the mechanical performance of the components, especially the cold-formed thin-walled steel components. The initial geometric imperfections mainly include global initial imperfections and local initial imperfections.

3.2.1 Global initial imperfections

After measurement, the global initial imperfection value of each specimen is shown in Table 3. It can be obtained from Table 3: (1) The global initial imperfection value of each specimen is less than 1/1000 of the length of specimen. (2) The maximum value of global initial imperfection appears on the web.

Table 3. Global initial imperfection value of each specimen

Specimen number	Component number	Amplitude e/mm	Amplitude/Length e/L	Specimen number	Component number	Amplitude e/mm	Amplitude/Length e/L
SP-1	MB-1-A	1.27	1/3134	SP-4	MB-4-A	0.80	1/4975
	MB-1-B	0.92	1/4326		MB-4-B	1.62	1/2457
SP-2	MB-2-A	0.48	1/8292	SP-5	MB-5-A	1.46	1/2726
	MB-2-B	0.16	1/24875		MB-5-B	2.67	1/1494
SP-3	MB-3-A	2.35	1/1694	SP-6	MB-6-A	0.34	1/11706
	MB-3-B	2.26	1/1761		MB-6-B	0.48	1/8292

3.2.2 Local initial imperfections

For the lipped C-section stainless steel beams, only two cross-sectional sizes were selected for the measurement of local initial imperfections (C250×75×20×2.0 and C250×75×20×2.5), and the length of the specimen was 920 mm. Three specific sections along the length of each specimen were selected, as shown in Fig. 4 (a). Seven measuring points were arranged for each flange edge, and 13 measuring points were arranged for the web edge, as shown in Fig. 4 (b). The measurement along the length only included the initial imperfection distribution on the centreline corresponding to the midpoints on each side of the specimen section, as shown in points A, B and C in Fig. 4 (b). There were 24 measuring points in each centreline, and the distance between the measuring points was set at 20 mm.

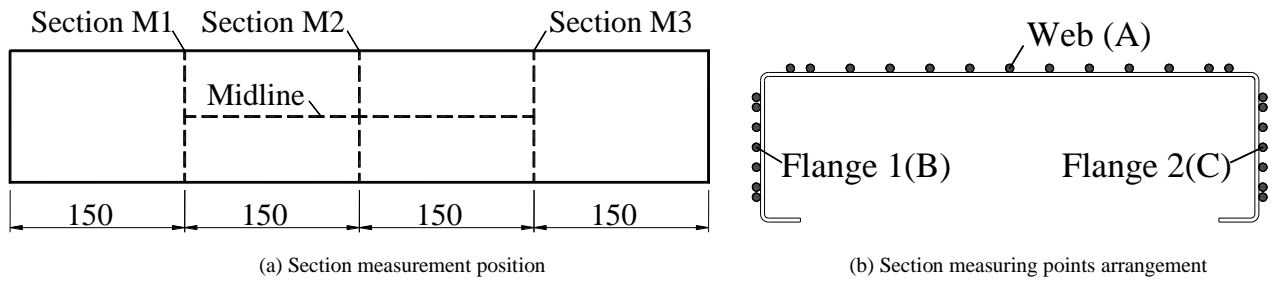


Fig.4 Section measurement position and measuring points arrangement for local initial imperfections of specimen

The distribution of initial imperfections in the cross section of each specimen is shown in Fig. 5. The distribution of the initial imperfections along the length direction of the centreline is shown in Fig. 6. The results of the maximum value of imperfections of each specimen are shown in Table 4.

Based on Figs. 5 and 6 and Table 4, the following conclusions can be drawn: (1) For the initial imperfection of the specimen, the maximum amplitude is basically located in the middle of the web; (2) Except for specimen C250×75×20×2.5, the amplitude of the initial imperfection of the other specimens is below 1/1000 of the corresponding measurement length; and (3) For the initial imperfections along the length direction of the centreline of the specimen, the amplitudes of the web and flange centreline are below 1/5000 of the measured length, and the initial imperfections in the length direction of the specimen are smaller.

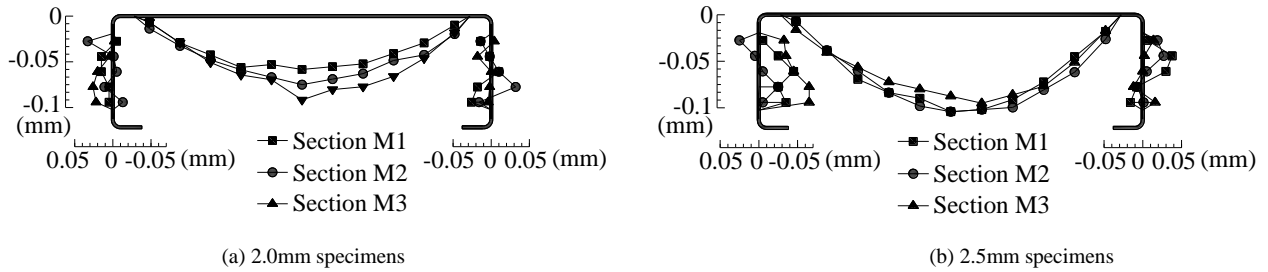


Fig.5 Initial imperfection distribution in the cross section

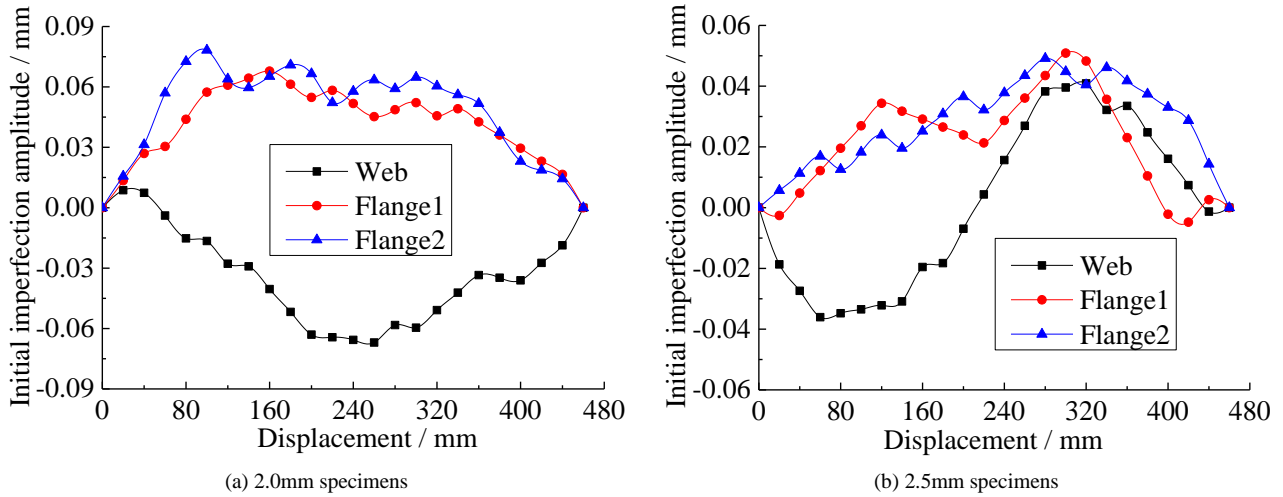


Fig.6 Initial imperfection distribution along the length of the center line

Table 4. Maximum value of imperfections of each specimen

Section number	Initial imperfection type	Geometric imperfection position	Measurement value Δ /mm	Δ/L
C250×75×20×2.0	Imperfection in the cross-section	Web	0.1100	1/2000
		Flange 1	0.0330	1/1515
		Flange 2	0.0320	1/1562
	Imperfection along length	Web midline	0.0670	1/6866
		Flange 1 midline	0.0678	1/6784

		Flange 2 midline	0.0783	1/5874
C250×75×20×2.5	Imperfection in the cross-section	Web	0.1250	1/1760
		Flange 1	0.0650	1/769
		Flange 2	0.0380	1/1316
	Imperfection along length	Web midline	0.0409	1/11264
		Flange 1 midline	0.0509	1/9037
		Flange 2 midline	0.0491	1/9369

3.3 Test of the bending capacity around the strong axis

3.3.1 Loading device

In the test of bending capacity around strong axis of the stainless steel lipped C-section beam, two-point loading was adopted. Meanwhile, to ensure global stability of the specimen, angle steel $\angle 60 \times 5$ were provided between the tension flanges of the double C-section component members of the specimen, and were connected to the double C-section component members by bolts, as shown in Fig.7.

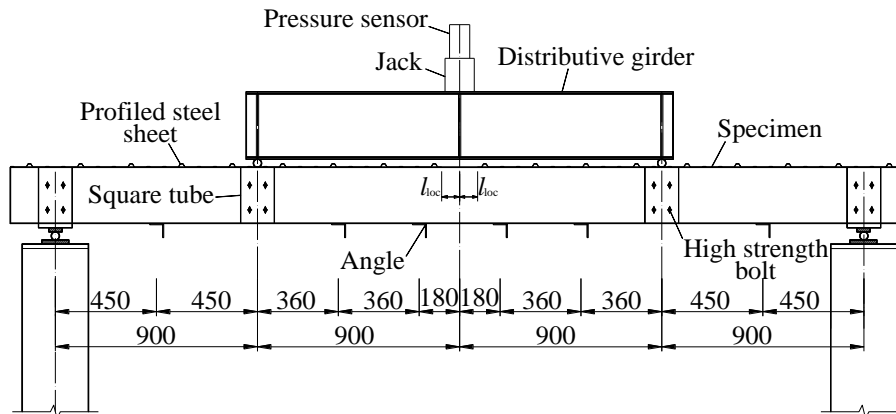


Fig.7 Strong axis bending test device

During the test, the constraint conditions of the two ends of the supports are: one end was fixed hinged and the other end was one-way sliding.

3.3.2 Layout of test equipment

To obtain the load-displacement curve of each specimen during the test, 8 displacement meters were arranged on the specimen, as shown in Fig. 8(a). The displacement meters DS5 ~ DS8 were

mainly used to monitor the rotation angle of the two ends, and DS1 ~ DS4 were mainly used to measure the vertical displacement of the specimen.

At the same time, in order to investigate the stress distribution of the cross-section of the specimen, five strain gauges were pasted on the inner and outer sides of the mid-span section of each specimen, located at the upper and lower flanges and the web, as shown in Fig.8 (c). The number in brackets in the figure is the strain gauge number inside the section of the specimen.

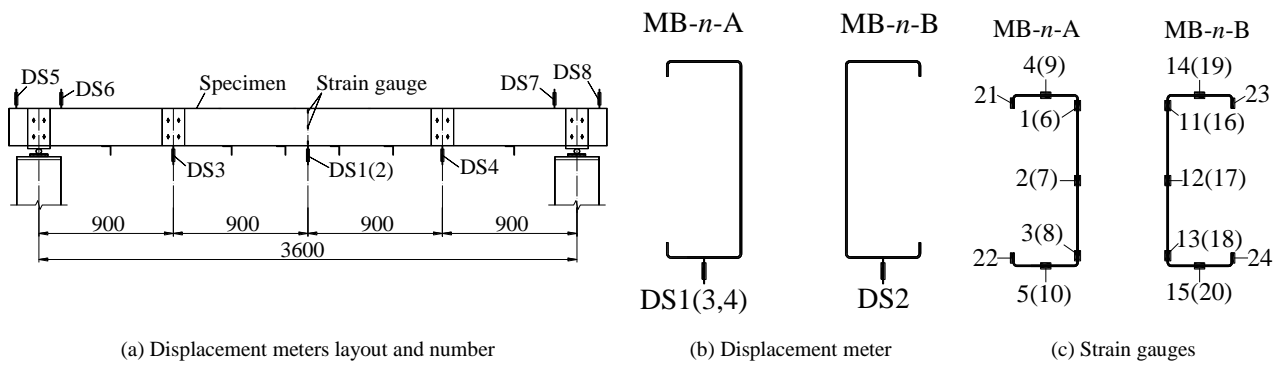


Fig.8 Layout of displacement meters and strain gauges on specimen

3.3.3 Test phenomenon

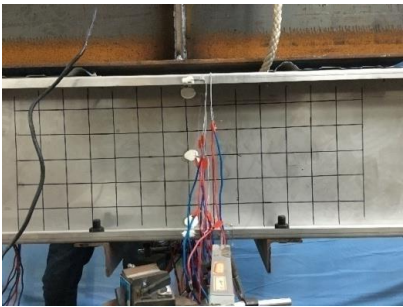
During the test of the local buckling bearing capacity of specimens SP-1 ~ SP-6, the test phenomena were similar. Due to space limitations, only specimen SP-2 is reported on here.

The test phenomena occurred as follows. At the beginning, the webs of MB-2-A and MB-2-B gradually underwent local buckling, and the half wave buckling amplitude was small. When the load increased further, the half wave of the mid span web of MB-2-A became more pronounced, and the flange of MB-2-B became concave due to local buckling. When the load reached 60.38 kN, an upward convex buckling half wave was shown on the flange of the mid span section of MB-2-A, as shown in Fig. 9 (b).

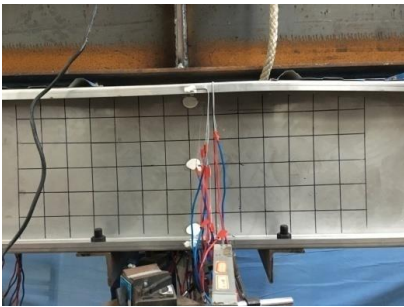
When the ultimate bearing capacity reached 65.86 kN, the buckling half waves of the flange and

1 web of MB-2-A and MB-2-B were more pronounced; local buckling in the flange only occurred in the
 2 section at the mid span or in the position that marginally deviated from the mid span; and the buckling
 3 amplitude was greater than that of the web, as shown in Fig. 9 (c) and (d), respectively. Results showed
 4 that eleven half waves were formed on the web of a single member from the mid-span to two loading
 5 points, and the deformation was symmetric about the mid-span section. The deformation of MB-2-A
 6 and MB-2-B is anti-symmetric.

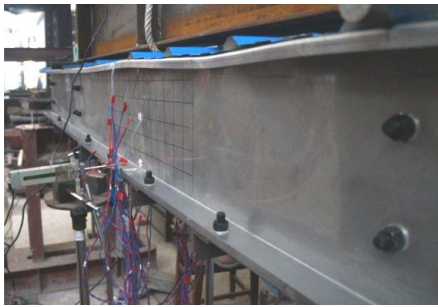
7 After reaching the ultimate bearing capacity, the flange of MB-2-A at one side of the mid span
 8 was concave, and the amplitude increased. The web at the concave section exhibited marked
 9 concaveness, and the amplitude of the buckling wave was quickly greater than that of the web plate at
 10 the mid span, as shown in Fig. 9 (e). The flange of MB-2-B at one side of the mid span was convex,
 11 and the amplitude of the upward convex was greater than that of the flange in mid. Concurrently, local
 12 buckling of the web at the upper convex section occurred rapidly, and the buckling amplitude was
 13 greater than that of the web at the mid span, as shown in Fig. 9 (f).



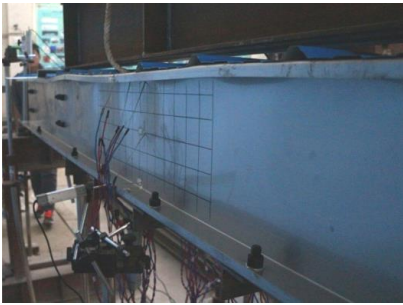
(a) $P=0\text{kN}$ (MB-2-A)



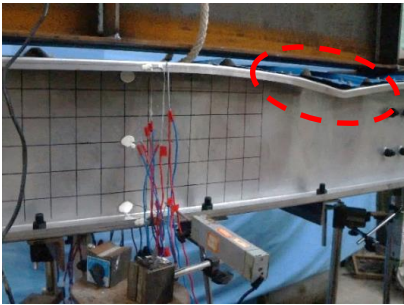
(b) $P=60.38\text{kN}$ (MB-2-A)



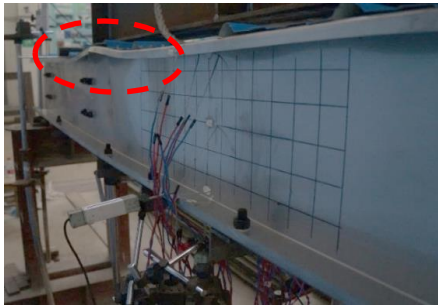
(c) $P=65.86\text{kN}$ (MB-2-A)



(d) $P=65.86\text{kN}$ (MB-2-B)



(e) $P=48.86\text{kN}$ (MB-2-A)



(f) $P=48.86\text{kN}$ (MB-2-B)

Fig.9 Test phenomenon of specimen SP-2

3.3.4 Test results

For specimens SP-1~SP-6, results, including the load-vertical displacement curve, load-strain curves of the web and flange, load-strain curve of the web, load-strain curve of the flange and local buckling bearing capacity of each specimen, were determined.

1. Load-displacement curve

The load-vertical displacement curves are shown in Fig.10. The vertical displacement is the average value of the mid-span displacements of the two components MB-n-A and MB-n-B.

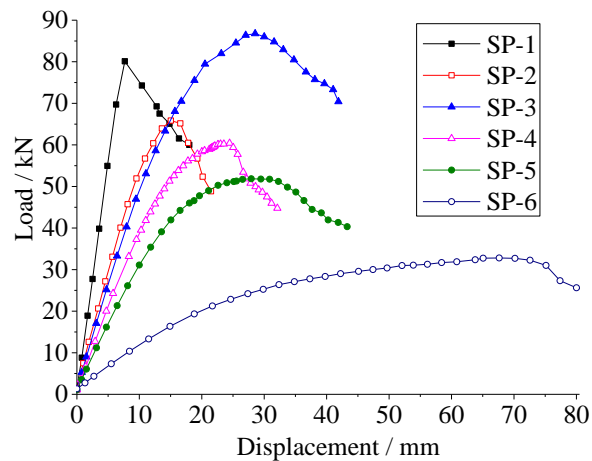


Fig.10 Load-vertical displacement curves

Fig. 10 shows that the trends of the load-displacement curve of the other specimens are similar, except for SP-1. In the initial stage, the mid-span displacement increases linearly with the load. As the load increases, the stiffness of the specimen decreases, and the load-displacement curve is nonlinear. After the extreme load point, the load gradually decreases, and the displacement increases continuously until the specimen fails. Additionally, near the extreme load point, the mid-span displacement of the specimen increases rapidly, the load changes slowly, and the specimen shows marked ductility. Last, in SP-1, the section height is the largest, the test is the most difficult, and the loading rate is too fast

because SP-1 is the first specimen in this test; thus, the load displacement curve decreases quickly after the load reaches the maximum value and does not show marked ductility.

2. Load- strain curve of web and flange

The load-strain curves of the web and flange are shown in Fig. 11 (a)-(f). Due to space limitations, only the curves of measuring points located on component MB-n-A are shown. The curve of component MB-n-B is similar to that of MB-n-A.

Fig. 11 shows that the upper flange and upper area of the web were approximately uniformly compressed at the initial stage of loading, and the load-strain curve of each measuring point was linear. After reaching the ultimate bearing capacity, the load-strain curve exhibited different trends, which indicated that the flange and web of the specimen present different local buckling modes. For SP-2, the strain of the upper flange and the inner and outer areas of the upper web (points A ~ D) of the mid span section were transformed from the compressive state to the tensile state, which indicated that local buckling occurred on the flange and the upper area of the web, and the peak or trough of the buckling half wave was not in the mid span section. For SP-5, the strain on the inner side of the upper flange (point A) of the mid span section developed to the compressive state with a large change range, and the strain on the outer side (point B) transformed from the compressive state to the tensile state, indicating that local buckling with upward convexity occurred on the upper flange. The strain of the inner (point C) and outer (point D) sides of the upper area of the web transformed from the compressive state to the tensile state, and the change range of the lateral strain was greater than that of the inner one, indicating that local buckling occurred on the upper area of the web.

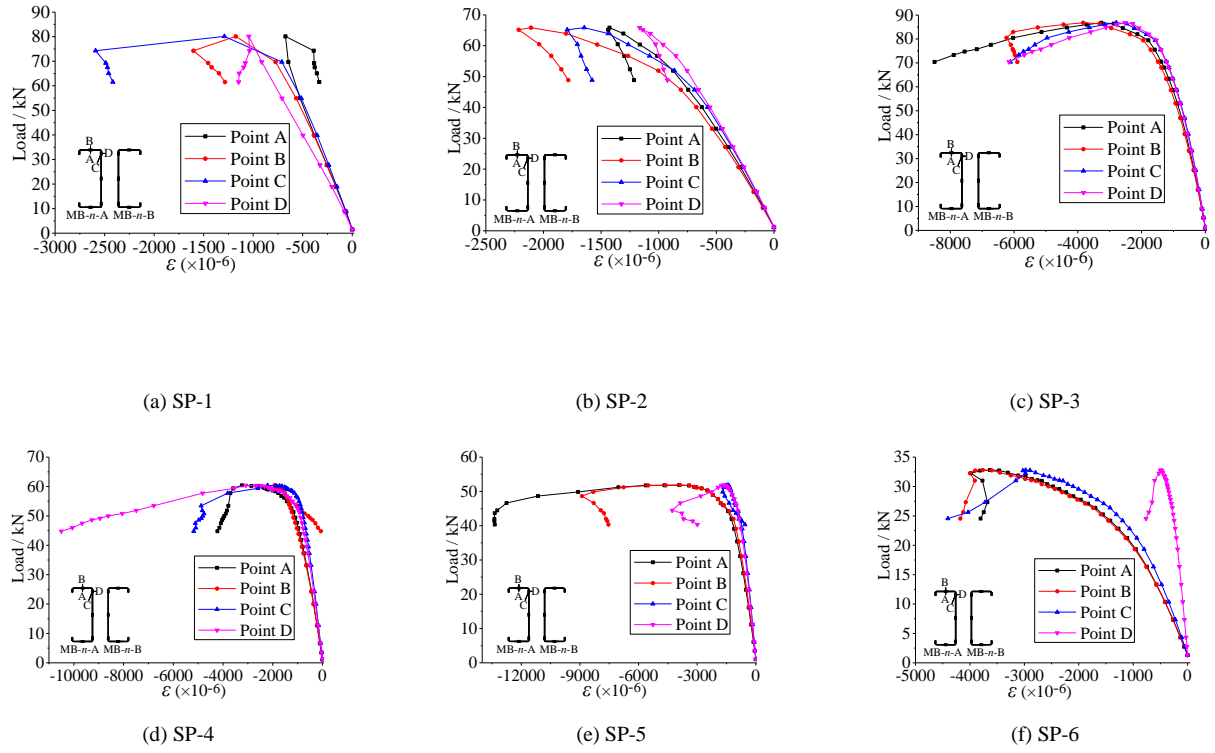
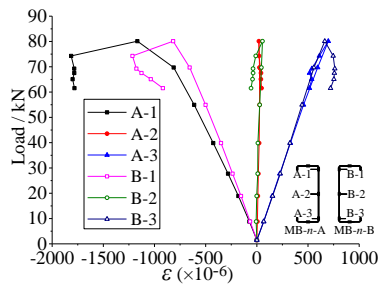


Fig.11 Load-strain curve of web and flange of specimens SP-1~SP-6 (only including member MB-n-A measuring point)

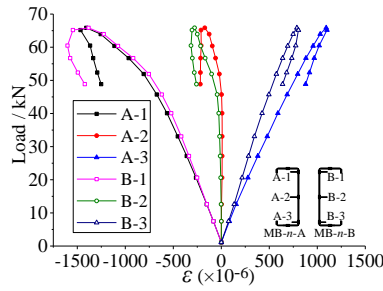
3. Load- strain curve of web

The load-strain curves of the webs of MB-n-A and MB-n-B are shown in Fig. 12(a)-(f), respectively.

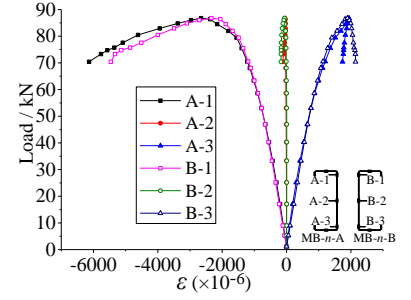
Fig. 12 shows that in the early stage, the strain of the middle area of the webs on the mid-span section was near zero, and the load-strain curves at the upper and lower points of the web were nearly symmetrical, indicating that the mid-span section was in a pure bending state. The curves of the two C-section members nearly coincided, indicating that the two members were subjected to the same stress. In the later stage, the web curves of the two members exhibited similar trends, indicating that the two members could still work together well.



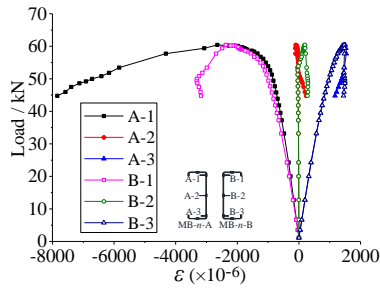
(a) SP-1



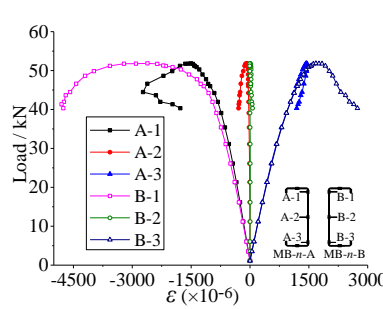
(b) SP-2



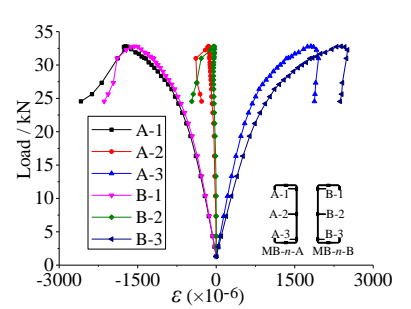
(c) SP-3



(d) SP-4



(e) SP-5

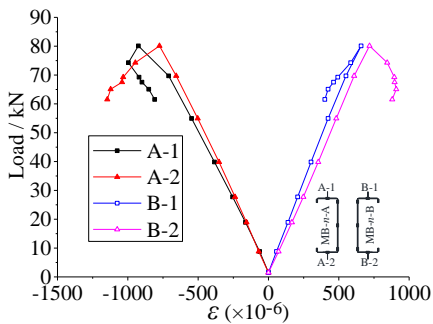


(f) SP-6

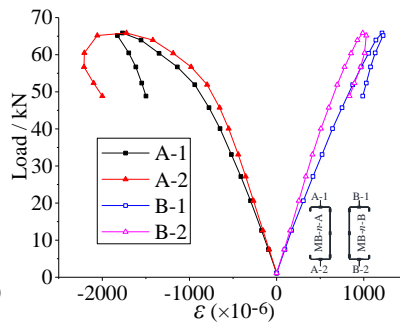
Fig.12 Load-strain curve of web of specimens SP-1~SP-6

1 4. Load- strain curve of flange

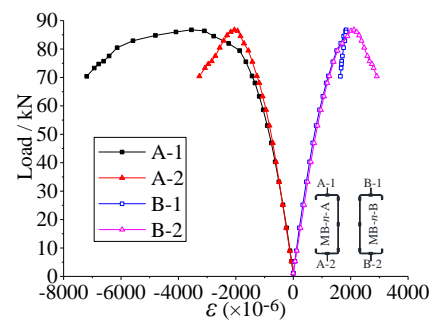
2 The load-strain curves of the flange of members MB-n-A and MB-n-B are shown in Fig. 13(a)-
3 (f), respectively.



(a) SP-1



(b) SP-2



(c) SP-3

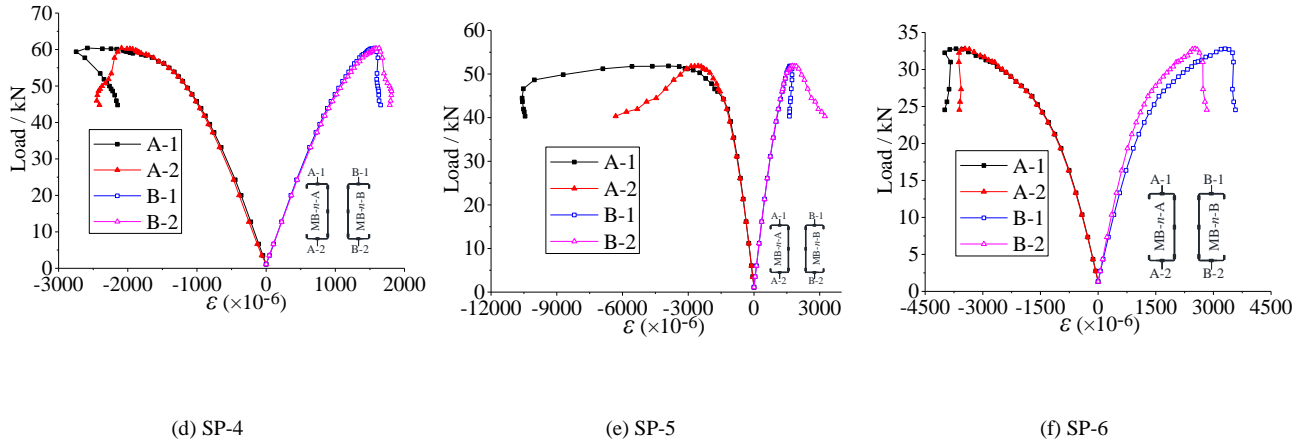


Fig.13 Load-strain curve of flange of specimens SP-1-SP-6

Fig. 13 shows that in the early stage, the load-strain curves of the upper and lower flanges on the mid-span section were nearly symmetric, indicating that the mid-span section was in a pure bending state. The curves of the two C-section members nearly coincided, indicating that the two members were subjected to the same force. In the later stage, the curves of MB-n-A and MB-n-B also exhibited similar trends, indicating that the two components could still work together well.

5. Local buckling bearing capacity

The ultimate bearing capacity and local buckling moment are shown in Table 5, where P_u is the test value of the ultimate bearing capacity; M_{test} is the local buckling moment of the single member MB-n-A or MB-n-B; M_y is the yield moment; M_{crl} is the critical moment of elastic local buckling; M_{crd} is the critical moment of elastic distortional buckling; and M_y , M_{crl} and M_{crd} can all be calculated and obtained by the finite strip software CUFSM.

Table 5. Test results of the bearing capacity and local buckling moment of each specimen

Specimen number	Component number	P_u/kN	$M_{test}/\text{kN}\cdot\text{m}$	$M_y/\text{kN}\cdot\text{m}$	$M_{crl}/\text{kN}\cdot\text{m}$	$M_{crd}/\text{kN}\cdot\text{m}$	M_{test}/M_y
SP-1	MB-1-A	80.11	18.02	32.73	14.04	19.53	0.55
	MB-1-B		18.02	33.04	14.28	20.04	0.55
SP-2	MB-2-A	65.86	14.82	20.89	15.53	19.00	0.71
	MB-2-B		14.82	21.05	16.17	19.56	0.70
SP-3	MB-3-A	86.77	19.52	20.18	34.56	30.70	0.97
	MB-3-B		19.52	20.27	34.99	30.61	0.96

SP-4	MB-4-A	60.42	13.59	16.10	17.70	18.95	0.84
	MB-4-B		13.59	15.88	17.18	18.59	0.86
SP-5	MB-5-A	51.85	11.67	12.74	14.48	19.38	0.92
	MB-5-B		11.67	12.75	14.32	19.18	0.92
SP-6	MB-6-A	32.81	7.38	7.04	17.65	14.84	1.05
	MB-6-B		7.38	6.94	16.83	14.41	1.06

Based on Table 5, the following conclusions can be drawn. First, the critical moment of elastic local buckling of other specimens was below that of elastic distortional buckling, except in SP-3 and SP-6. Thus, only local buckling occurred in the test. Second, for SP-3 and SP-6, the critical moment of elastic local buckling was greater than that of elastic distortional buckling; however, no distortional buckling occurred in the test, which indicated that the profiled steel sheet on the compression flange could better limit the occurrence of distortional buckling. Last, for SP-6, the ratio of the local buckling moment to the yield moment M_{test}/M_y was greater than 1.0, which showed that when reaching the ultimate bearing capacity, the section of the specimen yielded. For SP-1 ~ SP-5, M_{test}/M_y was below 1.0, which showed that local buckling failure had occurred before the section yielded.

4. Numerical simulation analysis

A refined finite element model was developed using the finite element software ABAQUS and Python to simulate the local buckling and failure modes of specimens SP-1~SP-6. Simulation results were compared to the test results, and a simplified model was created based on these results.

4.1 Refined finite element model

4.1.1 Geometric model

In the model, the bolt and self-tapping screw were simplified and S4R shell element was used to simulate the C-section member, profiled steel sheet, square tube and angle steel. The model of each

component was completely consistent with the specimen. When the grid element was divided, the size of the element should not exceed 25 mm in both horizontal and longitudinal (axial) dimensions. For the C-section specimen, the difference of material mechanical properties between the flat and corner area should be considered, and the mesh should be divided into two different areas.

4.1.2 Material model

In the model, a two-stage expression for the stress-strain relationship of stainless steel proposed by Gardner [35] was adopted as the stress-strain curve, as shown in Eq. (1). The material parameters were taken from the test results of flat and corner coupons.

$$\varepsilon = \begin{cases} \frac{\sigma}{E_0} + 0.002 \left(\frac{\sigma}{\sigma_{0.2}} \right)^n & 0 \leq \sigma \leq \sigma_{0.2} \\ \frac{\sigma - \sigma_{0.2}}{E_{0.2}} + \left(\varepsilon_{t1.0} - \varepsilon_{t0.2} - \frac{\sigma_{1.0} - \sigma_{0.2}}{E_{0.2}} \right) \left(\frac{\sigma - \sigma_{0.2}}{\sigma_{1.0} - \sigma_{0.2}} \right)^{n'_{0.2,1.0}} + \varepsilon_{t0.2} & \sigma_{0.2} < \sigma \leq \sigma_u \end{cases} \quad (1)$$

Where, $n'_{0.2,1.0}$ is the strengthening index.

4.1.3 Constraints and load application

In the finite element model, the square tube and the web, the angle steel and the lower flange, the profiled steel sheet and the flange were connected with bolts or self-tapping screws using the beam constraint in the multipoint constraint (MPC).

To simplify the model, the square tube at the support and the two C-section members had the same height; thus, the rigid binding constraint (Rigid Tie) was applied to the lower edge boundary of the square tube and the reference point, and a displacement constraint was used to the reference point. The rotation constraint (UR1) in the length direction had to be released at one end of the model to achieve the fixed hinge constraint condition. The translational constraint in the length direction and the rotation

constraint in the width direction (U3 and UR1) had to be released at the other end to achieve the sliding hinge constraint condition.

In the model, the load was applied using the displacement loading method, and the displacement load was primarily applied to the specimen at the reference point. At the loading point, the upper edge boundary of the square tube was rigidly bound to the reference point. No constraint was set between the reference point and the two C-section members and the profiled steel sheet to prevent stress concentration.

4.1.4 Initial geometric imperfection

To compare with the test results of specimens SP-1~SP-6, the test results describing the imperfection amplitude were used as the initial geometric imperfection, as shown in Table 4. The imperfection distribution mode of the first-order elastic buckling mode was used.

4.2 Finite element results

To verify the accuracy of the model, the finite element results and the test results were compared, including the failure mode, the load-displacement curve and the ultimate bearing capacity of each specimen.

4.2.1 Failure mode

Regarding the failure mode of the specimen, a comparison between the test results and the finite element results is shown in Fig. 14. Only the results of specimens SP-2 and SP-6 are shown because, SP-1 is the same as SP-2, and SP-3~SP-5 are the same as SP-6.

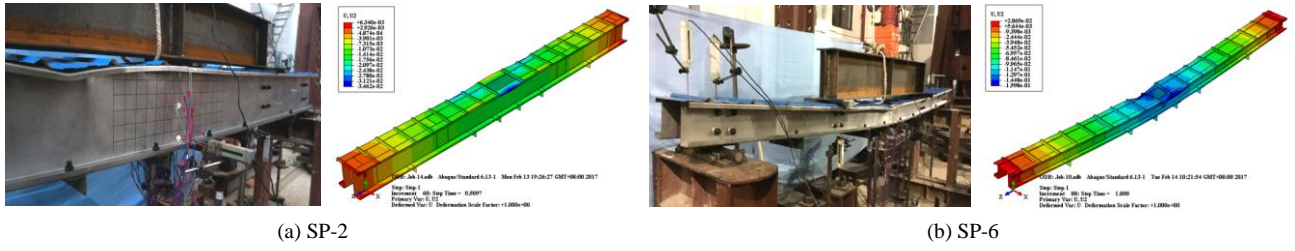


Fig.14 Comparison between test results and finite element results of failure mode of specimen

Fig. 14 shows that the test results for specimens SP-3~SP-6 were in good agreement with the finite element results, and local buckling and final failure both occurred in the region that was twice the half wavelength in the mid-span. For specimens SP-1 and SP-2, errors were present. In the test results, the local buckling amplitude at the position of mid-span deviating from the loading point was the largest, and was greater than that at the mid-span section. In the finite element results, local buckling only occurred in the mid-span area. For specimens SP-1~SP-6, the test results of the buckling wave shape and number were completely consistent with the finite element results.

4.2.2 Load-displacement curve

A comparison of the load-displacement curves of SP-1~SP-6 between the test results and the finite element results is shown in Fig. 15(a) and (b).

Fig. 15 shows that for SP-2~SP-6, the test results were in good agreement with the finite element results and showed marked ductility. In the early stage, the finite element results of the initial stiffness of the specimens were in good agreement with the test results. In the later stage, the finite element results of the initial stiffness were marginally above the test results. Additionally, errors were present in the results of specimen SP-1.

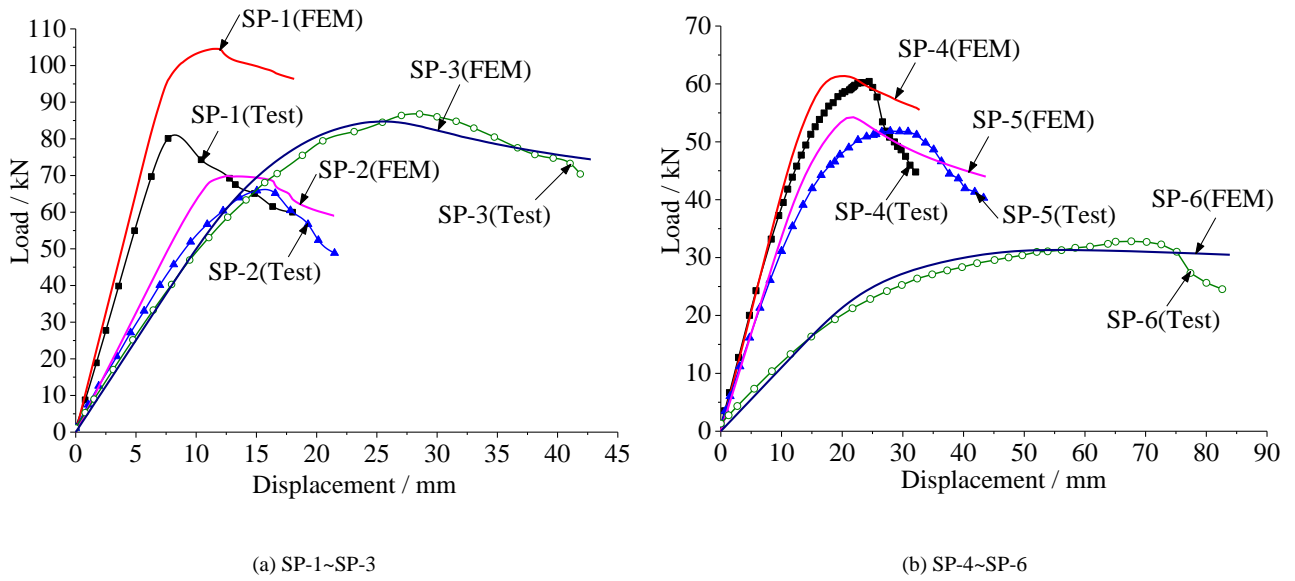


Fig.15 Comparison of load-displacement curve between test results and finite element results of specimens

4.2.3 Ultimate bearing capacity

Regarding the ultimate bearing capacity of SP-1~SP-6, a comparison between the test results and the finite element results is shown in Table 6.

Table 6. Comparison of ultimate bearing capacity between test results and finite element results

Specimen number	Section	Test P_T /kN	Finite element P_{FE} /kN	Error	P_{FE}/P_T
SP-1	C400×90×20×2.0	80.11	104.56	30.52%	1.31
SP-2	C300×80×20×2.0	65.86	70.26	6.68%	1.07
SP-3	C250×75×20×2.5	86.77	84.74	-2.34%	0.98
SP-4	C250×75×20×2.0	60.42	61.36	1.56%	1.02
SP-5	C250×50×20×2.0	51.85	54.25	4.63%	1.05
SP-6	C150×60×20×2.0	32.74	31.32	-4.34%	0.96
Average error				3.91%	1.01

Note: The average error in the table is the error that does not include SP-1 calculation result, and the absolute value is used for calculation.

Table 6 shows that the finite element results of the ultimate bearing capacity of other specimens were in good agreement with the test results, except for SP-1. The average error was 3.91%, and the maximum error was 6.68%. For SP-1, the error was 30.52%.

For stainless steel lipped C-section beams under strong axis bending, the refined finite element model yielded accurate simulations of mechanical performance.

4.3 Simplification model

4.3.1 Constraint simplification model

1. Simplification model

In the previously refined finite element model, the constraints between the steel angle and the lower flange of the members are so complex that they require considerable computational time, preventing a parametric analysis. In this case, three different models were developed to consider the effect of angle steel on the local buckling capacity of bending members. In the first model, which established a finite element model based on real dimensions, the angle steel was connected with the lower flange of the member through the beam constraint connection in MPC, denoted as GM-A. In the second model, without including the angle steel, the steel angle was replaced by a link constraint connection in MPC, denoted as GM-B. In the third model, the angle steel was removed, and no constraints were used at the lower flange of the two members, denoted as GM-C.

To investigate the effects of the amplitudes of initial imperfection on the bearing capacity, four different amplitudes of imperfection were selected: no initial imperfection (No II), initial imperfection 1 (II1), initial imperfection 2 (II2), and initial imperfection 3 (II3). II1, II2 and II3 are the amplitudes of local imperfections measured in practice and the values of imperfections that lie at 25% and 75% of the cumulative distribution function for initial imperfection, respectively. Based on the results of references [33], the values of initial imperfection that lie at 25% and 75% of the cumulative distribution function for initial imperfection are $0.14t$, where t is the thickness of the lipped C-section members, and $0.66t$, respectively. Based on 3 different models and 4 different imperfection conditions, 6 constraint simplification models (CSMs) were developed, and denoted CSM1~CSM6. Each CSM and its corresponding model and amplitudes of imperfections are shown in Table 7.

Table 7. Constrain simplification model information

Constrain simplification model	CSM1	CSM2	CSM3	CSM4	CSM5	CSM6
Geometric model	GM-A	GM-B	GM-C	GM-A	GM-A	GM-A
Imperfection	No II	No II	No II	II1	II2	II3

To verify the accuracy of the CSM, simulations were performed to describe the mechanical properties of specimens SP-1~SP-6. Simulation results were then compared to test results, including load-displacement curves and ultimate capacities.

2. Comparison of Load-Displacement Curves

The load-displacement curve for each specimen was obtained by CSM. A comparison of specimens SP-2 and SP-6 are shown in Fig. 16(a) and (b).

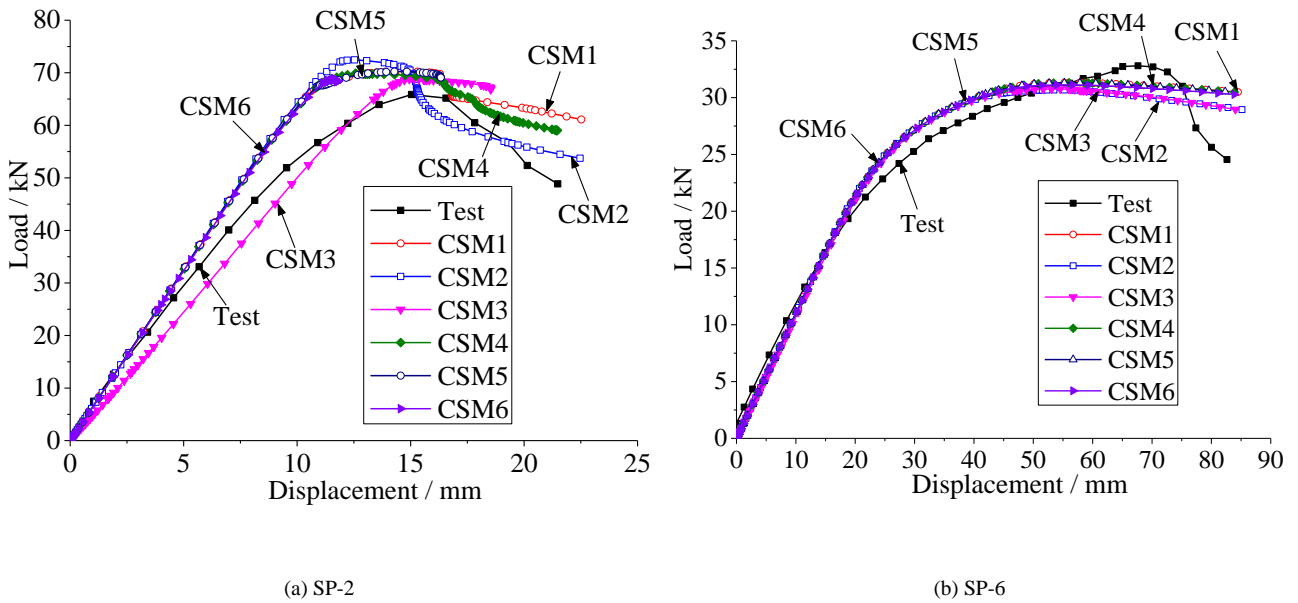


Fig.16 Comparison of load-displacement curve between finite element results and test results

Fig. 16 shows that the results obtained by CSM match well with the test results for specimens SP-2 and SP-6. For the initial stiffness in the early stage, the results of CSM1, CSM2 and CSM4~ CSM6 match well with the test results. In the later stage, the results of CSM3 match well with the test results. Additionally, in the early stage, the load-displacement curves obtained for CSM1 and CSM4~ CSM6 are similar, and little difference is observed in the later stage. Results show that the initial imperfection

has little effect on the load displacement curve of the specimen at the later stage.

3. Comparison of Ultimate Capacity

The ultimate capacity of each specimen obtained from the finite element results and test results are shown in Table 8.

Table 8. Comparison of CSM results and test results

Specimen number	Test P_T /kN	Ultimate bearing capacity of CSM P_{FE} /kN											
		CSM1		CSM2		CSM3		CSM4		CSM5		CSM6	
		P_{FE} /kN	Error	P_{FE} /kN	Error	P_{FE} /kN	Error	P_{FE} /kN	Error	P_{FE} /kN	Error	P_{FE} /kN	Error
SP-1	80.11	105.40	31.57%	105.34	31.49%	101.33	26.49%	104.56	30.52%	104.48	30.42%	100.81	25.84%
SP-2	65.86	70.28	6.71%	72.45	10.01%	68.82	4.49%	70.26	6.68%	70.22	6.62%	68.79	4.45%
SP-3	86.77	84.74	-2.34%	84.28	-2.87%	83.31	-3.99%	84.74	-2.34%	84.72	-2.36%	84.86	-2.20%
SP-4	60.42	61.37	1.57%	61.24	1.36%	62.00	2.62%	61.36	1.56%	61.38	1.59%	61.61	1.97%
SP-5	51.85	54.46	5.03%	54.38	4.88%	54.17	4.47%	54.25	4.63%	54.04	4.22%	53.75	3.66%
SP-6	32.74	31.32	-4.34%	30.67	-6.32%	30.75	-6.08%	31.32	-4.34%	31.30	-4.40%	31.13	-4.92%
Average error			4.00%		5.09%		4.33%		3.91%		3.84%		3.44%

Note: The average error in the table doesn't include the error of specimen SP-1 and absolute value is used in calculation.

Table 8 shows that the ultimate capacities obtained by CSM match well with the test results for all specimens except SP-1. Among the CSMs with no initial imperfection (CSM1~3), the results of CSM1 match the best with the test results. The ultimate capacities of CSM4~5 are closer to the test results, and the results of CSM6 match the best with the test results.

Thus, the elimination of the steel angle only decreases the initial stiffness of the specimen in the model and has a small influence on the ultimate capacities of the specimen. The influence of the initial imperfection on the ultimate capacities of the specimen is also shown to be small, and the results of CSM3 match the best with test results. In this case, when analysing the local buckling capacity of a C-section stainless steel member under strong axis bending, CSM3 without a steel angle is recommended.

1 4.3.2 *Length simplification model*

2 1. *Simplification model*

3 For CSM, there are still many constraints between the upper flange of C-section members and the
4 profiled steel sheet. Thus, further simplification of the CSM is required.

5 Based on the experimental failure phenomenon of specimens SP-1 ~ SP-6, local buckling failure
6 primarily occurs in the range that is twice the local buckling half wavelength of the pure bending
7 section. Therefore, the finite element analysis model of the specimen was further simplified, and a
8 portion of the regions along the length of the specimen was selected for analysis. The model obtained
9 by this simplification method is called the length simplification model (LSM). Four methods are used
10 to determine the length in LSM. First, the pure bending length of the specimen is analysed. Based on
11 the constraint conditions of the self-tapping screw connection between the profiled steel sheet and the
12 upper flange of the C-section member, two simplification models are divided as follows. If the self-
13 tapping screw connection position is simplified by the link constraint of MPC, it is denoted as model
14 LSM1. If all self-tapping screw points are rigidly bound to the reference point, it is denoted as model
15 LSM2. Second, twice the local buckling half wavelength of the specimen is then analysed. Based on
16 the end constraint of the simplified specimen, the specimen is divided into a rigid constraint (LSM2.0-
17 1) and a hinged constraint (LSM2.0-2). Third, 2.5 times the local buckling half wavelength of the
18 specimen is analysed and divided into a rigid constraint (LSM2.5-1) and a hinged constraint (LSM2.5-
19 2). Last, three times the local buckling half wavelength of the specimen is analysed and divided into a
20 rigid constraint (LSM3.0-1) and a hinged constraint (LSM3.0-2).

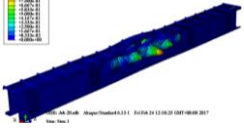
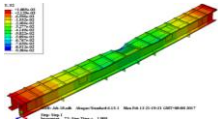
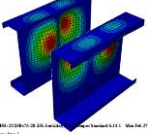
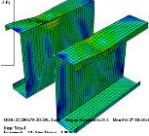
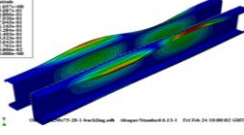
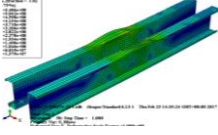
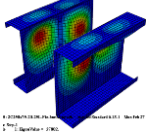
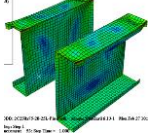
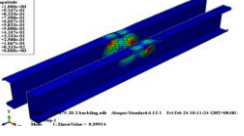
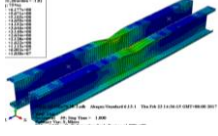
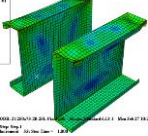
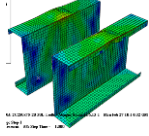
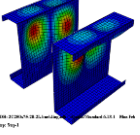
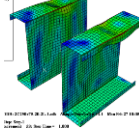
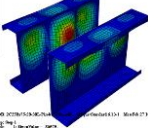
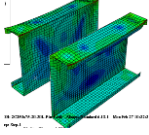
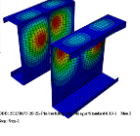
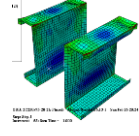
21 To verify the accuracy of LSM, simulations of the mechanical properties of specimens SP-1~SP-
22 6 are performed using these eight types of LSMs. The LSM results are compared to those of the refined

1 finite element model, including the failure modes, moment-curvature curve and local buckling capacity.

2 2. Comparison of Failure Modes

3 For specimens SP-1~SP-6, eight types of LSMs are used to perform simulations. The buckling
4 and failure modes of each specimen are similar, and only specimen SP-4 is selected as an example for
5 clarity, as shown in Table 9. The refined finite element model is denoted as SP-FM.

6 **Table 9. Results of buckling and failure modes obtained by different models (SP-4)**

Model	Buckling mode	Failure mode	Model	Buckling mode	Failure mode
SP-FM			LSM2.5-1		
LSM1			LSM2.5-2		
LSM2			LSM3.0-1		
LSM2.0-1			LSM3.0-1		
LSM2.0-2					

7 The following conclusions can be obtained from the results shown in Table 9. The results of LSM1
8 and LSM2 are shown to be different from those of SP-FM because the link constraint in LSM1 only
9 restricts the displacement of the upper flange along the width direction, while the rotation of the self-
10 tapping screw is not restricted. Rotation thus fails to act as an ideal constraint, resulting in distortional
11 buckling of the upper flange. In LSM2, the constraint on the upper flange of the specimen is so strong

that no deformation can occur in addition to the range within twice the length of the half-wavelength in the midspan. Local buckling only occurs in the mid span region; however, the local buckling mode agrees with the SP-FM results. Additionally, the buckling modes obtained by the rigid and hinged models are shown to be similar and in good agreement with the SP-FM results.

However, the failure modes of the rigid and hinged models are found to be different. For the rigid model, the local buckling of the flange and web only occurs in the mid span area. For the hinged model, local buckling occurs in the flange and web in the mid span area, as well as the flange near the support. In the rigid model, the flange and web near the support cannot deform due to the rigid constraint. Conversely, in the hinged model, the influence of the hinge constraint on the flange and web near the support is small, and multiple buckling half waves occur. Additionally, compared to the hinged model, the failure mode of the rigid model is more consistent with the SP-FM result.

3. Comparison of Moment -Curvature Curves

The moment-curvature curves of each specimen are obtained by the SP-FM model and eight types of model LSMs, as shown in Fig. 17.

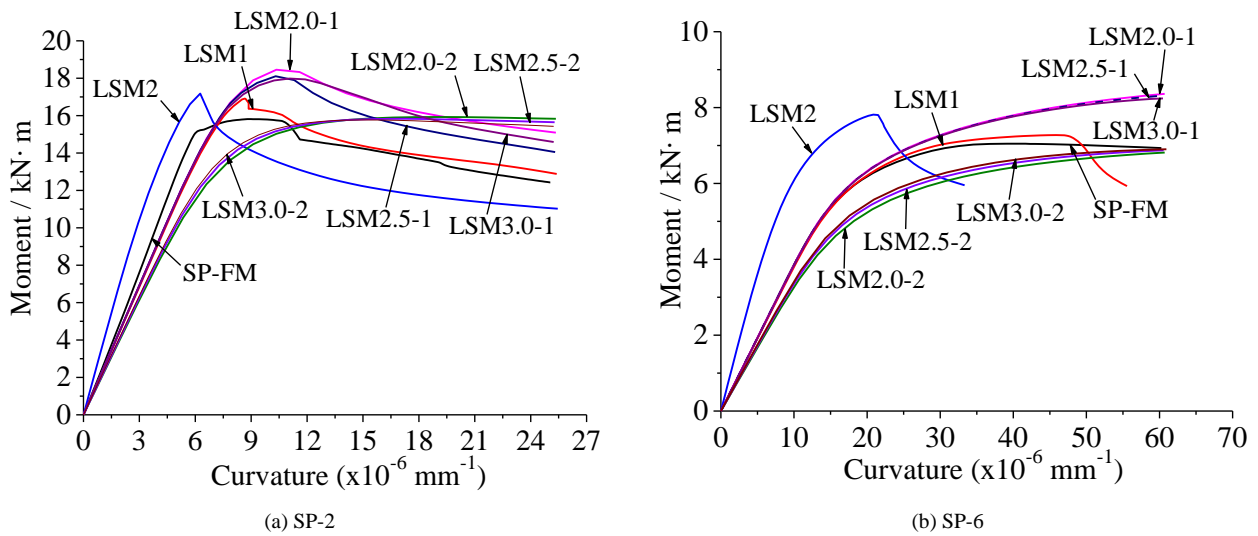


Fig.17 Comparison of results of moment-curvature curves

Fig. 17 shows that the initial stiffness obtained by LSM2 is greater than that of SP-FM for SP-2 and SP-6, while that of the hinged models is nearly equal and lower than that of SP-FM. For SP-2, LSM1 and rigid models exhibit nearly identical initial stiffnesses that are marginally below the results of SP-FM. For SP-6, the initial stiffness obtained by LSM1 and rigid models is nearly equal to that of SP-FM. Additionally, in the moment-curvature curve of the specimen, when the load reaches the ultimate bearing capacity, the curvature of the mid span section obtained by other models except LSM1 and LSM2 is greater than that of SP-FM. Thus, in the finite element analysis of strong axis beams, the rigid length simplification models can more accurately simulate the mechanical properties of the specimens.

4. Comparison of Local Buckling Capacity

For specimens SP-1 ~ SP-6, the local buckling bearing capacity was obtained by SP-FM and eight types of LSMs, as shown in Table 10.

Table 10. Local buckling ultimate bearing capacity of specimens SP-1~SP-6 obtained by different LSMs

Specimen number	Local buckling bearing capacity								
	Finite model	Length simplified model							
	SP-FM	LSM2.0-1	LSM2.0-2	LSM2.5-1	LSM2.5-2	LSM3.0-1	LSM3.0-2	LSM1	LSM2
SP-1	22.48	26.74	22.20	24.38	22.04	24.35	21.77	22.11	22.91
	—	18.97%	-1.23%	8.47%	-1.96%	8.33%	-3.14%	-1.63%	1.93%
SP-2	15.81	18.46	15.93	18.11	15.83	17.98	15.77	16.91	17.18
	—	16.76%	0.75%	14.55%	0.12%	13.73%	-0.25%	6.96%	8.67%
SP-3	19.07	21.92	18.37	21.46	18.22	20.50	18.05	18.78	19.86
	—	14.94%	-3.70%	12.53%	-4.47%	7.50%	-5.33%	-1.52%	4.14%
SP-4	13.81	15.38	12.91	15.05	12.85	14.81	12.81	13.62	14.40
	—	11.375	-6.49%	8.985	-6.98%	7.24%	-7.28%	-1.38%	4.27%
SP-5	12.25	13.07	11.59	12.77	11.27	12.53	11.11	11.95	12.24
	—	6.69%	-5.36%	4.24%	-8.00%	2.29%	-9.33%	-2.45%	-0.08%
SP-6	7.05	8.47	7.00	8.37	6.97	8.25	6.94	7.28	7.82
	—	20.14%	-0.72%	18.72%	-1.15%	17.02%	-1.57%	3.26%	10.92%
Average error		14.81%	-2.79%	11.25%	-3.74%	9.35%	-4.48%	0.54%	4.97%

Table 10 shows that among the LSMs, the local buckling bearing capacity obtained by model LSM1 is the closest to that of SP-FM, with an average error of 0.54%. The results obtained by LSM2 are marginally different from those of SP-FM, with an average error of 4.97%. Additionally, the local buckling capacities obtained by rigid models are all above that of SP-FM, and the shorter the length is, the larger the error by approximately 10%. Last, the local buckling bearing capacity obtained by the hinged models is below that of SP-FM, and the longer the length is, the larger the error by approximately 5%.

In conclusion, in LSM, specimen length affects the local buckling bearing capacity. Under the same support conditions, the simplification model with a longer length acquires a smaller local buckling bearing capacity. Additionally, the support conditions at both ends have a certain influence on the local buckling bearing capacity. Under the same length, the model with rigid connections acquires a larger local buckling bearing capacity than that with hinge connections.

4.3.3 Length Simplification Model with Initial Imperfection

To further investigate the accuracy of the LSM with initial imperfections based on these six types of LSMs, the local buckling bearing capacity of specimens SP-3 and SP-4 with initial imperfections was simulated. The amplitude of the initial imperfection is shown in Table 7, and three amplitudes of initial imperfection were considered: initial imperfection 1 (II1), initial imperfection 2 (II2) and initial imperfection 3 (II3). The local buckling bearing capacities of specimens SP-3 and SP-4 with different initial imperfections were obtained and are listed in Table 11.

Table 11. Local buckling bearing capacity of specimens with initial imperfection (SP-3 and SP-4) obtained by different LSMs

Analysis model	Contents	Local buckling bearing capacity M_{FE} and error /kN·m	
		SP-3	SP-4

		No II	II1	II2	II3	No II	II1	II2	II3
SP-FM	M_{FE}	19.07	19.07	19.06	19.09	13.81	13.81	13.81	13.86
LSM2.0-1	M_{FE}	21.92	21.43	20.96	19.39	15.38	15.04	14.77	13.68
	Error	14.94%	12.385	9.97%	1.57%	11.37%	8.94%	6.95%	-1.31%
LSM2.0-2	M_{FE}	18.37	18.37	18.38	18.43	12.91	12.92	12.93	13.07
	Error	-3.70%	-3.68%	-3.60%	-3.38%	-6.495	-6.45%	-6.39%	-5.70%
LSM2.5-1	M_{FE}	21.46	21.10	20.71	19.39	15.05	14.85	14.65	13.79
	Error	12.53%	10.645	8.66%	1.57%	8.98%	7.53%	6.08%	-0.52%
LSM2.5-2	M_{FE}	18.22	18.22	18.23	18.30	12.85	12.85	12.85	12.90
	Error	-4.47%	-4.47%	-4.43%	-4.03%	-6.98%	-6.95%	-6.95%	-6.92%
LSM3.0-1	M_{FE}	21.07	20.78	20.16	18.78	14.81	14.72	14.55	13.84
	Error	10.49%	8.97%	5.77%	-1.62%	7.24%	6.62%	5.35%	-0.16%
LSM3.0-2	M_{FE}	18.05	18.08	18.08	18.01	12.81	12.79	12.77	12.67
	Error	-5.33%	-5.21%	-5.21%	-5.58%	-7.28%	-7.34%	-7.52%	-8.60%

Table 11 shows that the local buckling capacities of the specimens obtained by other models exhibit errors compared to the results of SP-FM with the same imperfection amplitude, except for LSM3.0-2. These errors are shown to decrease with increasing imperfection amplitude. Additionally, as the imperfection amplitude changes, the local buckling capacity of specimens SP-3 and SP-4 obtained by models SP-FM and LSM3.0-2 show marked irregularity.

In the eight types of LSMs, models LSM1 and LSM2 are inappropriate for finite element analysis with arbitrary cross-section dimensions and different experimental conditions due to their fixed length. For LSM2.5-2, the local buckling capacity is below that of SP-FM, and the results of the buckling mode, failure mode and moment-curvature curve all match well with that of SP-FM. Therefore, model LSM2.5-2 is the closest model to SP-FM and can thus simulate the mechanical properties of the stainless steel C-section beam under strong axial bending.

5. Conclusion

Based on S30408 austenitic stainless steel (AISI304), tests of the local buckling bearing capacity and numerical simulation analyses were performed on stainless steel lipped C-section beams under

strong axis bending. Comparing the test results and the results obtained by different analysis models, the following conclusions are obtained:

(1) The failure modes of all specimens are shown to be local buckling, and multi-wave local buckling occurs in the flange and web near the mid-span section.

(2) The trend of the load displacement curves are similar, and specimens exhibit marked ductility.

(3) Considering the models with different flange constraints and different initial imperfections, six types of CSMs are developed, which can simulate the failure modes of the specimen. In the model, the initial stiffness will decrease without the angle steel; however, the associated influence on the ultimate bearing capacity is small, as is that of the initial imperfection on the ultimate bearing capacity.

(4) Eight types of LSMs were developed to analyse the local bearing capacity. Results show that the length and constraint conditions of the support affect the local buckling capacity. Under the same support constraints, the local buckling calculated by LSM decreases with increasing specimen length. Under the same length conditions, the local buckling bearing capacity obtained by the LSM with rigid support is greater than that of the LSM with hinge support.

(5) In the eight types of LSMs, the local buckling bearing capacity obtained by LSM2.5-2 is marginally less than that of SP-FM; however, the results of the buckling mode, failure mode and moment-curvature curve are in good agreement with SP-FM. Therefore, model LSM2.5-2 can simulate the mechanical properties of the specimen accurately.

Acknowledgements

The authors gratefully acknowledge the financial support of and National Natural Science Foundation of China (No. 51878146 and No. 51378105). The research was supported by High level

talents of "six talent peaks" in Jiangsu Province (No. JZ-001) and Qing Lan Project of Jiangsu Province (2016). This financial support is gratefully acknowledged.

References

- [1] Kwon Y B, Hancock G J. Tests of cold-formed channels with local and distortional buckling [J]. *Journal of Structural Engineering*, 1992; 118(7): 1786-1803.
- [2] Tang J, Young B. Column tests of cold-formed steel channels with complex stiffeners [J]. *Journal of Structural Engineering*, 2002; 128(6):737-745.
- [3] Tang J, Young B. Compression tests of channels with inclined simple edge stiffeners [J]. *Journal of Structural Engineering*, 2002; 129(10):1403-1411.
- [4] Yu C, Schafer B W. Local buckling tests on cold-formed steel Beams[J]. *Journal of Structural Engineering*, 2003; 129(12): 1596-1606.
- [5] Yu C, Schafer B W. Distortional buckling tests on cold-formed steel beams [J]. *Journal of Structural Engineering*, 2006; 132(4): 515-528.
- [6] Mohammad R H, David A N. Local and distortional buckling of cold-formed steel beams with edge-stiffened flanges [J]. *Journal of Constructional Steel Research*, 2012; 73: 31-42.
- [7] Wang H M. Study on the stability behavior of cold-formed steel flexural members[D]. School of Civil and Engineering, Harbin Institute of Technology, Harbin, 2009.
- [8] Zhang Y. Performance research on local buckling and distortional buckling of cold-formed thin-wall C-Section steel flexural members[D]. College of Civil and Engineering, Chongqing University, Chongqing, 2009.
- [9] Landesmann A, Camotim D. Distortional failure and DSM design of cold-formed steel lipped channel beams under elevated temperatures[J]. *Thin-Walled Structures*, 2016, 98:75-93.
- [10] He Z Q, Zhou X H, Zou B, Chen P. Calculation-method investigation on ultimate load-carrying capacities of cold-formed steel columns experiencing distortional-global buckling interaction under axial compression[J]. *Journal of Building Structures*, 2019, 40(3):192-199.
- [11] Gardner L, Nethercot D A. Experiments on Stainless Steel Hollow Sections- Part 2: Members Behaviour of Columns and Beams [J]. *Journal of Constructional Steel Research*, 2004; 60(9): 1319-1332.
- [12] Lecce M, Rasmussen K J R. Distortional buckling of cold-formed stainless steel sections: Experimental investigation. *Journal of Structural Engineering*, 2006; 132(4): 497-504.
- [13] Lecce M, Rasmussen K J R. Distortional buckling of cold-formed stainless steel sections: Finite element modeling and design. *Journal of Structural Engineering*, 2006; 132(4): 505-514.
- [14] Feng Z, Young B. Cold - formed stainless steel sections subjected to web crippling [J]. *Journal of Structural Engineering*, 2006; 132(1): 134-144.
- [15] Feng Z, Young B. Experimental investigation of cold-formed high-strength stainless steel tubular members subjected to combined bending and web crippling [J]. *Journal of Structural Engineering*, 2007; 133(7):1027-1034.
- [16] Becque J, Rasmussen K J R. Experimental investigation of local-overall interaction buckling of stainless steel lipped channel columns. *Journal of Constructional Steel Research* 2009; 65(8-9): 1677-1684.
- [17] Becque J, Rasmussen K J R. Numerical investigation of local-overall interaction buckling of stainless steel lipped channel columns. *Journal of Constructional Steel Research* 2009; 65(8-9): 1685-1693.
- [18] Rossi B, Jaspart J P, Rasmussen K J R. Combined distortional and overall flexural-torsional buckling of cold-formed stainless steel sections: Experimental investigations. *Journal of Structural Engineering*, 2010; 136(4): 354-360.

- [19] Rossi B, Jaspart J P, Rasmussen K J R. Combined distortional and overall flexural-torsional buckling of cold-formed stainless steel sections: Design. *Journal of Structural Engineering*, 2010; 136(4): 361-369.
- [20] Yuan H X. Local and local-overall buckling behavior of welded stainless steel members under axial compression[D]. Civil Engineering, Tsinghua University, Beijing, 2014.
- [21] Niu S, Rasmussen K J R, Asce M, Feng F. Local-global interaction buckling of stainless steel I-beams. I: Experimental investigation[J]. *Journal of Structural Engineering*, 2015; 141(8): 04014194.
- [22] Niu S, Rasmussen K J R, Asce M, Feng F. Local-global interaction buckling of stainless steel I-beams. II: Numerical study and design[J]. *Journal of Structural Engineering*, 2015; 141(8): 04014195.
- [23] Fan S G, Liu F, Zheng B F, Shu G P, Tao Y L. Experimental study on bearing capacity of stainless steel lipped C section stub columns [J]. *Thin-Walled Structures*, 2014; 83:70-84.
- [24] Fan S G, Tao Y L, Zheng B F, Liu F. Capacity of stainless steel lipped C-section stub column under axial compression [J]. *Journal of Constructional Steel Research*, 2014; 103(12): 251-263.
- [25] Haidarali M R, Nethercot D A. Finite element modelling of cold-formed steel beams under local buckling or combined local/distortional buckling[J]. *Thin-Walled Structures*. 2011,49(12): 1554-1562.
- [26] Cheng Y. Distortional buckling of cold-formed steel members in bending[R]. Research Report, American Iron and Steel Institute, Committee on Specifications, 2005.
- [27] National Standard of the People's Republic of China. Technical specification for stainless steel structures (CECS 410-2015). Beijing, China planning press; 2015.
- [28] National Standard of the People's Republic of China. Technical code of cold-formed thin-wall steel structures (GB50018-2002). Beijing, China planning press; 2002.
- [29] Technical Guide for Cold-Formed Steel Framing Products. Steel Framing Industry Association, 2012.
- [30] NAS. North American Specification for the design of cold formed steel structures: Appendix 1: Design of cold-formed steel structural members using the direct strength method. Washington (DC), American Iron and Steel Institute; 2004.
- [31] ASCE. Specification for the design of cold-formed stainless steel structural members. American Society of Civil Engineers, SEI/ASCE-8-02, Reston, Virginia, 2002.
- [32] Gardner L. A new approach to stainless steel structural design[D]. PhD Thesis. Department of Civil and Environmental Engineering, Imperial College, London, 2002.
- [33] Schafer B W, Peköz T. Computational modeling of cold-formed steel: characterizing geometric imperfections and residual stresses[J]. *Journal of Constructional Steel Research*. 1998, 47(3): 193-210.